

3D Macroporous Mo_xC@N-C with Incorporated Mo Vacancies as Anodes for High-Performance Lithium-Ion Batteries

Shenghong Liu, Feng Li, Dan Wang, Chunmao Huang, Yanming Zhao, Jong-Beom Baek,* and Jiantie Xu*

High electronic conductivity, low average working voltage, and high theoretical capacities enable molybdenum carbide-based materials as promising anodes for lithium-ion batteries (LIBs). Apart from the increase in the number of additional active sites, further enhancement in the specific activity of the active sites is also an effective way to improve the electrochemical performance of the molybdenum carbide-based electrodes. Here, a series of 3D cross-linked macroporous Mo_xC@N-C nanocrystals with rich incorporated Mo vacancies, high specific activity of active sites, and nitrogen-doped carbon (N-C) coating are designed and synthesized using a simple method. Benefitting from its 3D robust structures for the rapid transporting and additional storage of Li⁺, the Mo_xC@N-C-2.5 displays a high initial reversible capacity of 879.3 mAh g⁻¹ at 0.05 A g⁻¹. Moreover, the Mo_xC@N-C-2.5 shows a high discharge capacity of 825.3 mAh g⁻¹ at 0.5 A g⁻¹ with an initial capacity retention of 61.9% after 200 cycles. As expected, this facile strategy can be extended to the fabrication of other nanocomposites with rich defects, numerous porous structures, and heteroatoms doped carbon coating as electrodes toward high-performance LIBs.

Spurred by the overwhelming domination in the market of portable and smart devices (e.g., MP3, camera, and computers), rechargeable lithium-ion batteries (LIBs) have been considered as one of lead technologies for the large scale applications of electric vehicles (EVs) and stationary energy-storage systems (ESSs).^[1] To meet the high-demands of future EVs and ESSs, rapid development of advanced LIBs with much higher capacity, power, and energy density is urgently needed. It is commonly recognized that the performance of electrode material largely determines the success to the development of advanced LIBs.^[2] Although graphite as the mostly used anode has achieved great success in the market of LIBs, its relatively low theoretical capacity of 372 mAh g⁻¹ and poor rate capability largely restrict its further applications in the EVs and ESSs.^[3] As a result, a large number of alternatives have been developed, including C-family

based anodes (e.g., carbonaceous materials,^[4,5] Si,^[6] Ge,^[7] and Sn^[8]), N-family anodes (e.g., P,^[9] Sb,^[10] and Bi^[11]), transition metal oxides,^[12] transition metal sulfides,^[13] Li₄Ti₅O₁₂,^[14] and transition metal carbides (TMCs).^[15] Among them, TMCs as anodes for LIBs have already attracted tremendous attention, though the TMCs are mainly applied in the catalytic fields,^[16] such as oxygen reduction reaction (ORR),^[17] oxygen evolution reaction (OER),^[18] and hydrogen evolution reaction (HER).^[19] Since the first report on the Ti₂C as anode for LIBs in 2012,^[20] a series of TMCs with encouraging anode performance have been reported, including 2D layered carbides (e.g., Ti₂C,^[20] Ti₃C₂,^[21] V₂C,^[22] Nb₂C,^[23] and Cr₂C^[24]), and nonlayered carbides and their hybrids (e.g., Mo_{0.654}C,^[25] Mo₂C/C hybrids,^[26] Fe₂O₃/Fe₃C/graphene,^[27] and Mo₂C/N-doped carbon heteronano-wires^[28]). In particular, high electronic conductivity ($\approx 1.02 \times 10^2$ S cm⁻¹), appropriate average working voltages (≈ 1.0 V vs Li⁺/Li) and high theoretical capacities (>600 mAh g⁻¹) enable molybdenum carbide-based electrodes as emerging alternatives to graphite.^[15,29]


Despite the outstanding anode features for LIBs, bulk molybdenum carbide-based electrodes often suffer from poor cycle life and low rate capability. In order to achieve the high-performance molybdenum carbide-based anodes, two effective

S. Liu, C. Huang, Prof. J. Xu
Guangdong Provincial Key Laboratory of Atmospheric Environment and Pollution Control
School of Environment and Energy
South China University of Technology
Guangzhou 510640, China
E-mail: jiantie.xu@scut.edu.cn

S. Liu, C. Huang, Prof. Y. Zhao
School of Physics
South China University of Technology
Guangzhou 510640, China

Dr. F. Li, Prof. J.-B. Baek
School of Energy and Chemical Engineering/Center for Dimension-Controllable Organic Frameworks
Ulsan National Institute of Science and Technology (UNIST)
50 UNIST, Ulsan 44919, South Korea
E-mail: jbbae@unist.ac.kr

Prof. D. Wang
State Key Laboratory of Organic-Inorganic Composites
Beijing University of Chemical Technology
Beijing 100029, China

 The ORCID identification number(s) for the author(s) of this article can be found under <https://doi.org/10.1002/smt.201800040>.

DOI: 10.1002/smt.201800040

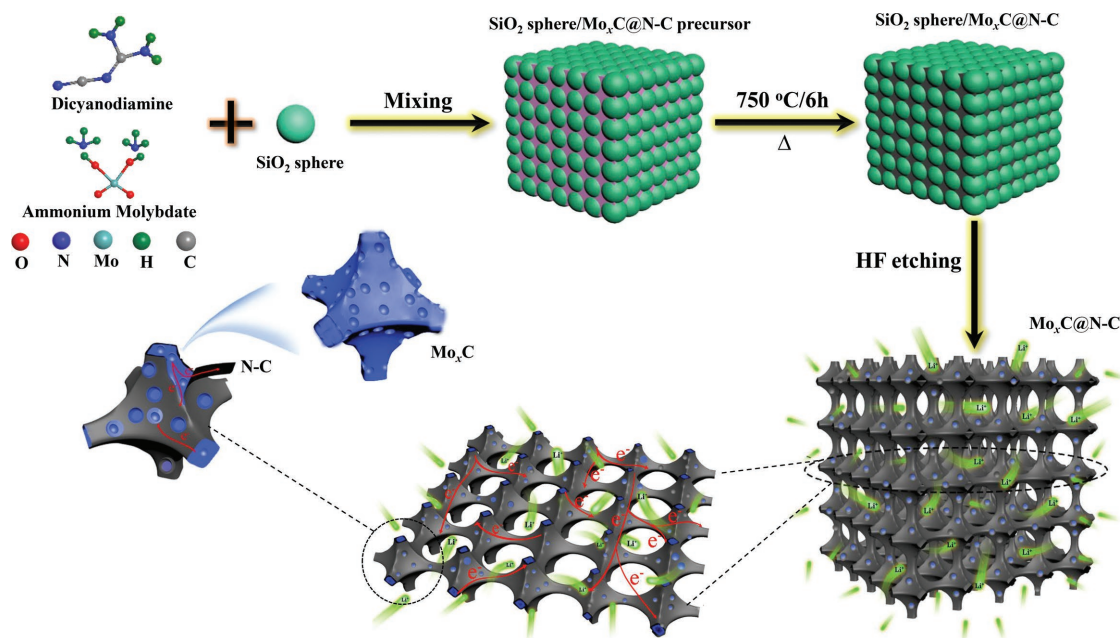


Figure 1. Scheme of the fabrication process of Mo_xC@N-C.

strategies have been widely adapted. One is the fabrication of molybdenum carbides with nanostructures (e.g., hierarchically porous and nanowire Mo₂C^[30–32]) and another one is hybridization of the molybdenum carbides with highly conductive agents (e.g., Mo₂C/graphene^[33] and Mo₂C/N-doped carbon^[34]). The former enables the molybdenum carbides with a large surface area and high pore volume, leading to quick penetration of electrolyte, rapid diffusion of ions, and numerous active sites for ions storage. The latter favors molybdenum carbide-based hybrids with improved electronic conductivity, reduced particle size and strain buffer within the hybrid, and effectively prevents the electrode from aggregating during the cycles. Besides, the two strategies are also often used in combination to further improve the electrochemical performance, such as mesoporous Mo₂C/C hybrid nanospheres^[26] and mesoporous Mo₂C/N-doped carbon heteronanowires.^[34] On the other hand, many studies have revealed that the presence of defects in the electrode materials could provide extra active sites for ions storage, thereby leading to the improved specific capacity.^[35] To obtain the defect-rich structures, many efforts have been devoted to increasing the number of additional active sites induced by the defects within the structures (e.g., heteroatoms doping and porous structures). Apart from the increase in the number of additional active sites, further enhancement in the specific activity of these active sites is also an effective way to improve the electrochemical performance of the active materials.

Herein, we designed and synthesized a series of Mo_xC@N-C nanocrystals with rich incorporated Mo vacancies, high specific activity of active sites, 3D cross-linked macroporous nanostructure, and nitrogen-doped carbon (N-C) coating (**Figure 1**). Benefitting from its unique robust and high activity structures, the Mo_xC@N-C displays outstanding lithium storage properties. This is because the Mo_xC@N-C nanocrystals with rich incorporated Mo vacancies and N-C could provide numerous

active sites with high specific activity exposure to Li⁺ storage. Moreover, both 3D cross-linked macroporous structure and N-C coated on the surfaces of Mo_xC@N-C effectively provide large accessible surface area and rapid transport channels for electrolyte penetration and Li⁺ (electrons) transporting, and prevention of the electrode aggregation during the cycles (**Figure 1**).

Figure 1 shows the preparation scheme of defect-rich Mo_xC@N-C with cross-linked macroporous nanostructures. First of all, dicyanamide (DCA) and ammonium heptamolybdate (AHM) with different mass ratios were mixed with SiO₂ spheres and then annealed at 750 °C for 6 h in nitrogen atmosphere. After that, the obtained mixture was leached in HF to completely remove the template of SiO₂ spheres. During this process, the interfaces between (molybdenum carbide)@N-C and SiO₂ were significantly modified along with the removal of strong-linker Mo–O–Si and simultaneous introduction of plenty of defects in Mo_xC and N-C. Compared to pure carbon (C), heteroatoms (especially, N)-doped carbon (N-C) enables N-C or their related hybrids as electrodes for LIBs with superior lithium storage properties.^[36] This is because that the well-bonded N-C not only significantly enhance the electronic conductivity of the electrode but also provide more nitrogen-containing active sites for the interaction between Li⁺ and C/N-C. In our experiments, additional N-C originated from the precursor of Mo_xC@N-C is expected to be coated on the surfaces of the Mo_xC@N-C. The amounts of N-C are depended on the mass ratio of the DCA/AHM (1.5/2.5/3.5). The resulted Mo_xC@N-C samples are named as Mo_xC@N-C-1.5, Mo_xC@N-C-2.5, and Mo_xC@N-C-3.5. For comparison, the commercial Mo₂C (Sigma) was also investigated.

The crystal structures of the Mo₂C, Mo_xC@N-C-1.5, Mo_xC@N-C-2.5, and Mo_xC@N-C-3.5 were identified by the X-ray diffraction (XRD) technique. As shown in **Figure 2a**, all the peaks of three Mo_xC@N-C samples are almost indexed to the characteristic peaks of MoC (ICSD #77157) and carbon

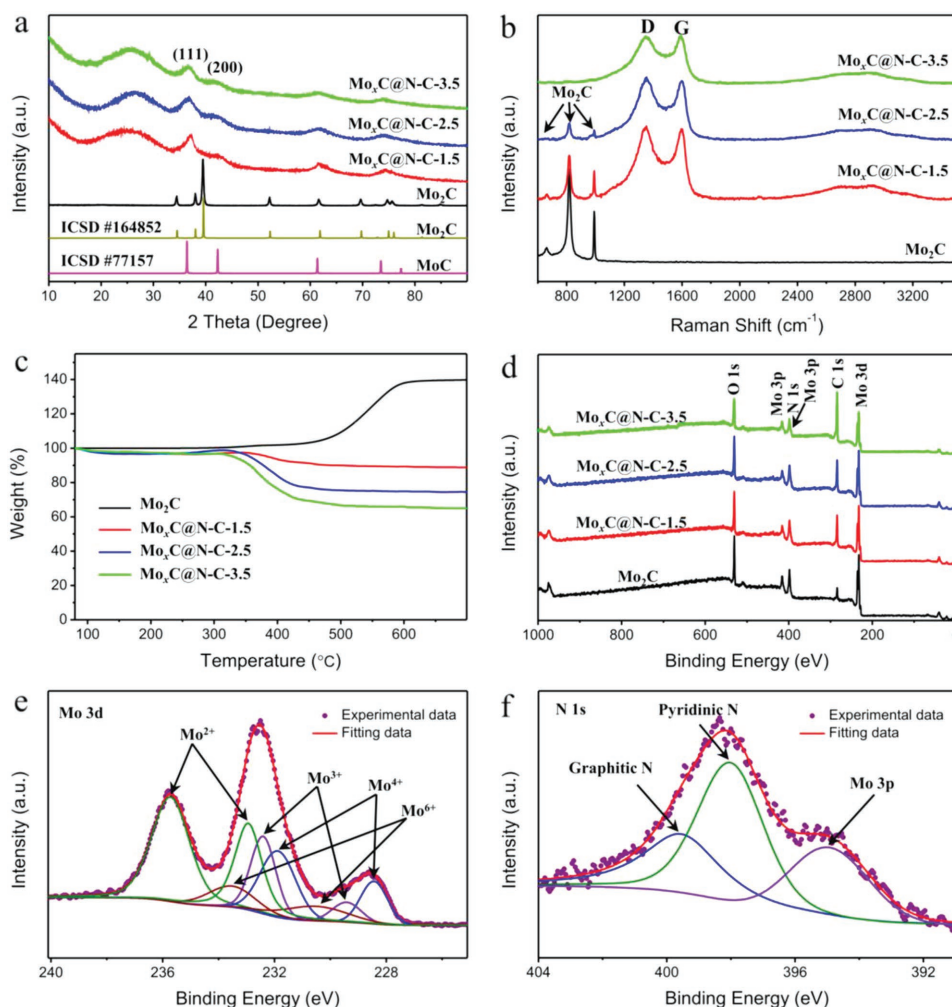


Figure 2. a) XRD patterns of Mo_xC , Mo_2C , $\text{Mo}_x\text{C@N-C-1.5}$, $\text{Mo}_x\text{C@N-C-2.5}$, and $\text{Mo}_x\text{C@N-C-3.5}$. b–d) Raman spectra, TGA curves, and XPS spectra of Mo_2C , $\text{Mo}_x\text{C@N-C-1.5}$, $\text{Mo}_x\text{C@N-C-2.5}$, and $\text{Mo}_x\text{C@N-C-3.5}$. High-resolution XPS spectra of $\text{Mo}_x\text{C@N-C-2.5}$ of e) Mo 3d and f) N 1s.

(26°). These characteristic peaks with broad band and low intensity are most likely due to the amorphous patterns and rich defects for $\text{Mo}_x\text{C@N-C}$. With the mass ratio of DCA/AHM from 1.5 to 3.5, the intensity ratio of characteristic peaks ($\text{Mo}_x\text{C/N-C}$) is obviously decreased. This is consistent with the results of Raman spectra (Figure 2b). As can be seen, all the $\text{Mo}_x\text{C@N-C}$ display two typical carbon peaks located at 1351 cm^{-1} (D band) and 1594 cm^{-1} (G band), which are attributed to the crystal defect or disordered graphite, and graphitic lattice vibration mode with E_{2g} symmetry, respectively.^[5] Apart from the carbon peaks, there are several other peaks at 662 , 817 , and 992 cm^{-1} , which are deviated from the characteristic peak of MoC ^[37] and almost well assigned to Mo_2C .^[30b] Together with the XRD result, it indicates the existence of rich Mo vacancies in the Mo_xC with $x = 1\text{--}2$. Similar to the XRD result, with the mass ratio of the DCA/AHM increases, the Raman peaks of Mo_xC become weaker and even disappear. The disappearance of Mo_xC peaks is mainly due to the disorder patterns of Mo_xC and increased amounts of disorder carbon (N-C). To estimate the carbon content, thermogravimetric analysis (TGA) of the $\text{Mo}_x\text{C@N-C}$ was carried out in air atmosphere. When x is

assumed as 2 (1), the carbon contents in the Mo_xC ($\text{Mo}_x\text{C@N-C-1.5}$, $\text{Mo}_x\text{C@N-C-2.5}$, and $\text{Mo}_x\text{C@N-C-3.5}$) are estimated to be 36.2 (32.5), 46.5 (43.3), and 52.8 (50.7) wt%, respectively (Figure 2c). The detailed calculation information are listed in Figure S1 and Equations (S1) and (S3) of the Supporting Information.

X-ray photoelectron spectroscopy (XPS) analysis was carried out to further investigate the elemental composition and oxidation states of $\text{Mo}_x\text{C@N-C}$. Figure 2d shows the full spectra of $\text{Mo}_x\text{C@N-C}$ with the binding energies of Mo 3d at $\approx 232\text{ eV}$, C 1s at $\approx 285\text{ eV}$, N 1s at $\approx 398\text{ eV}$, Mo 3p at $\approx 413\text{ eV}$ and O 1s at $\approx 530\text{ eV}$. The detailed element contents are listed in Table S1 of the Supporting Information. The high oxygen concentration is most likely due to the physically adsorbed and/or trapped oxygen and moisture on the surfaces of the samples. With the mass ratio of the DCA/AHM increases, the ratio of peak intensity (Mo 3d/C 1s) decreases, which agrees well with the results of XRD and Raman spectra. Based on the XPS results, the element contents of Mo in the Mo_2C , $\text{Mo}_x\text{C@N-C-1.5}$, $\text{Mo}_x\text{C@N-C-2.5}$, and $\text{Mo}_x\text{C@N-C-3.5}$ are 10.8, 8.2, 6.7, and 5.1 at%, respectively. As shown in Figure 2e and Figure S2

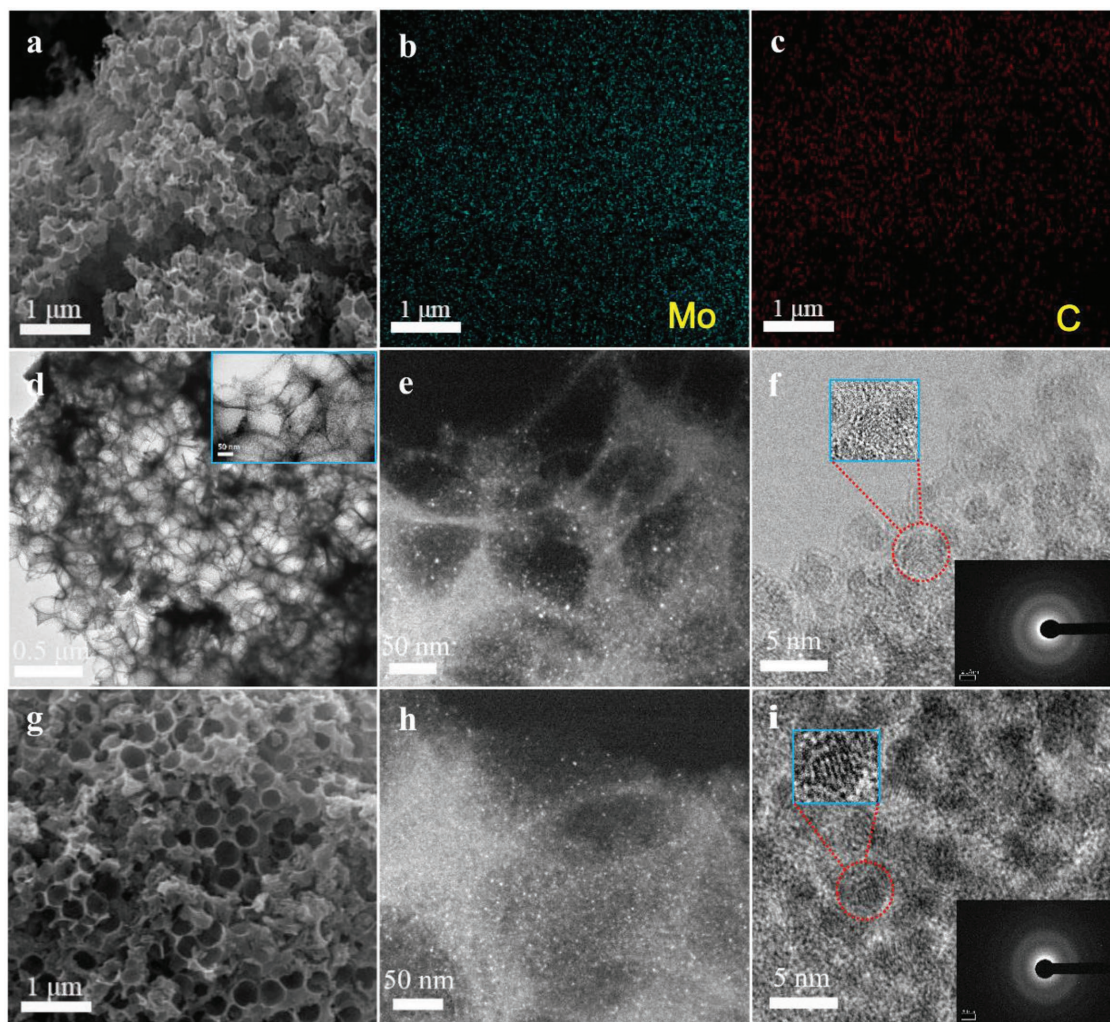


Figure 3. a) SEM image, corresponding elemental mapping of (a), b) Mo, and c) C. d,f) TEM and e) STEM images of $\text{Mo}_x\text{C}@N\text{-C-2.5}$. g) SEM image, h) STEM, and i) TEM images of $\text{Mo}_x\text{C}@N\text{-C-3.5}$. Insets of (d): magnified TEM image of $\text{Mo}_x\text{C}@N\text{-C-2.5}$. Insets of (f) and (i): SAED of (f) and (i).

(Supporting Information), high resolution XPS Mo peaks indicate that there are four valence states for Mo (i.e., Mo^{2+} , Mo^{3+} , Mo^{4+} , and Mo^{6+}) existing on the surfaces of the $\text{Mo}_x\text{C}@N\text{-C-1.5}$, $\text{Mo}_x\text{C}@N\text{-C-2.5}$, and $\text{Mo}_x\text{C}@N\text{-C-3.5}$, compared to only three valence states of Mo^{2+} , Mo^{4+} , and Mo^{6+} for Mo_2C . The Mo^{2+} , Mo^{4+} , and Mo^{6+} are attributed to the presence of $\text{MoO}/\text{Mo}_2\text{C}$, MoO_2/MoC , and MoO_3 in the Mo_xC , respectively. The existence of Mo^{3+} species in the $\text{Mo}_x\text{C}@N\text{-C}$ is mainly due to the appearance of Mo vacancies, which is resulted from the removal of SiO_2 and the breaking of Si–O–Mo bond at the interfaces between molybdenum carbides and SiO_2 during the leaching process. Because the Mo^{3+} is formed with changed charge-density distribution, the Mo^{3+} sites are expected to be more active to interact with other ions (i.e., Li^+). The Mo^{3+} signals from Mo in the $\text{Mo}_x\text{C}@N\text{-C-1.5}$, $\text{Mo}_x\text{C}@N\text{-C-2.5}$, and $\text{Mo}_x\text{C}@N\text{-C-3.5}$ are estimated to be 17.0%, 23.4%, and 19.6%, respectively, indicating more active sites in the $\text{Mo}_x\text{C}@N\text{-C-2.5}$ than $\text{Mo}_x\text{C}@N\text{-C-1.5}$ and $\text{Mo}_x\text{C}@N\text{-C-3.5}$. As shown in Figure 2f, the N 1s signal of from $\text{Mo}_x\text{C}@N\text{-C}$ is attributed to the precursor of DCA/AHM as the precursors, which can be

deconvoluted into pyridinic N at 398.1 eV and graphitic N at 399.6 eV,^[5] along with Mo 3p at 394.9 eV.^[19]

The morphologies and detailed structures of $\text{Mo}_x\text{C}@N\text{-C-2.5}$ and $\text{Mo}_x\text{C}@N\text{-C-3.5}$ were characterized by scanning electron microscopy (SEM) and transmission electron microscopy (TEM). As shown in Figure 3a,g, both $\text{Mo}_x\text{C}@N\text{-C-2.5}$ and $\text{Mo}_x\text{C}@N\text{-C-3.5}$ clearly display cross-linked macroporous structure with a pore size of ≈ 380 nm. The pore size equals to the diameter of the SiO_2 template. The macroporous structure and pore size can be also confirmed by TEM (Figure 3d). The elemental mappings (Figure 3b,c) obtained from the SEM image (Figure 3a) reveal that the Mo and C elements are homogeneously distributed through the whole structure. Moreover, the scanning TEM (STEM) images indicate the $\text{Mo}_x\text{C}@N\text{-C-2.5}$ (Figure 3e) and $\text{Mo}_x\text{C}@N\text{-C-3.5}$ (Figure 3h) with continuous interconnecting carbon frameworks and Mo-based dots entrapped inside the $\text{Mo}_x\text{C}@N\text{-C}$ structure. In addition, a trace amount of ultrafine nanocrystals (red-dotted circle in Figure 3f,i) can be found in the $\text{Mo}_x\text{C}@N\text{-C}$ structures. High-resolution TEM images indicate that the lattice spacing of nanocrystal is

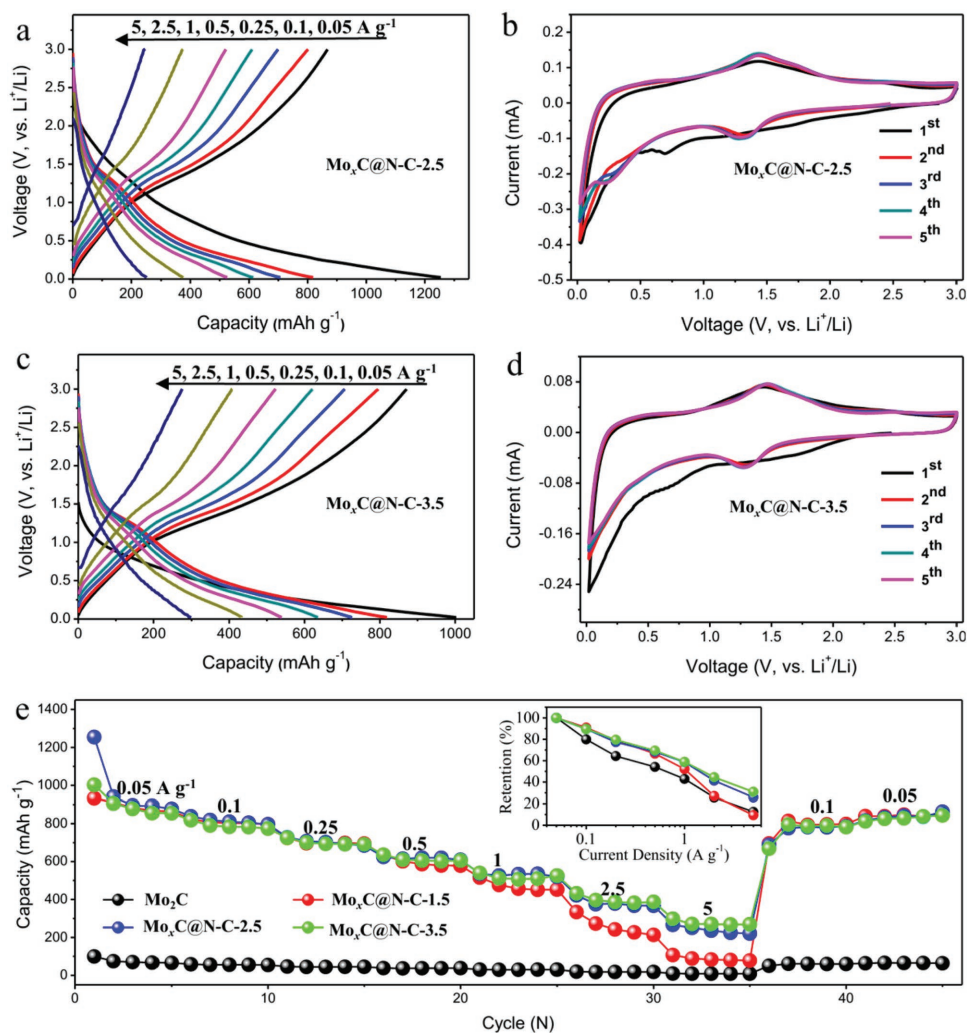


Figure 4. a,c) Discharge/charge profiles at various current densities and b,d) CV curves at 0.1 mV s^{-1} for initial 5 cycles of $\text{Mo}_x\text{C@N-C-2.5}$ and $\text{Mo}_x\text{C@N-C-3.5}$. e) Rate capability of Mo_2C , $\text{Mo}_x\text{C@N-C-1.5}$, $\text{Mo}_x\text{C@N-C-2.5}$, and $\text{Mo}_x\text{C@N-C-3.5}$. Inset of (e): capacity retention versus different current densities.

estimated to be $\approx 0.25 \text{ nm}$, corresponding to the (111) facet of MoC_{1-x} .^[32] It should be noted that the existence of part discontinuous lattice (point defects, red-dot circle in Figure 3f,i) and small nanocrystal size are responsible for the broaden of XRD peaks. This is consistent to the TEM result with an amorphous pattern (insets of Figure 3f,i).

Figure 4a,c and Figure S4 (Supporting Information) show the electrochemical behavior of Mo_2C , $\text{Mo}_x\text{C@N-C-1.5}$, $\text{Mo}_x\text{C@N-C-2.5}$, and $\text{Mo}_x\text{C@N-C-3.5}$ electrodes measured at 0.05 A g^{-1} in the voltage range of $0.02\text{--}3 \text{ V}$. As can be seen, the discharge-charge profiles are typical electrochemical behavior of molybdenum carbides, which agrees well with previous reports.^[30] Different from the $\text{Mo}_x\text{C@N-C}$ with distinct discharge-charge plateau at $\approx 1.4 \text{ V}$, the commercial Mo_2C exhibits a sloping discharge/charge curve, indicating its poor electrochemical kinetics. To further investigate the electrochemical behavior, cyclic voltammetry (CV) of the electrodes were measured at 0.1 mV s^{-1} for 5 cycles. As shown in Figure 4b,d, both $\text{Mo}_x\text{C@N-C-2.5}$ and $\text{Mo}_x\text{C@N-C-3.5}$ display a distinct peak that appears at $\approx 0.75 \text{ V}$

during the first cathodic scan. It is attributed to the formation of a solid state interface (SEI) layer on the electrode surface, as well as the Li^+ storage in the $\text{Mo}_x\text{C@N-C}$.^[30] In the following cycles, the disappearance of this peak for both $\text{Mo}_x\text{C@N-C-2.5}$ and $\text{Mo}_x\text{C@N-C-3.5}$ indicates the formation of a strong SEI layer in the first cycle. After the formation of SEI layer, more Li^+ are inserted into host structure below 0.75 V based on a combined mechanism ($x \text{ Li} + \text{Mo}_x\text{C} \rightarrow \text{Li}_x\text{C} + x \text{ Mo}$ and $x \text{ Li} + \text{N-C} \rightarrow \text{Li}_x(\text{N-C})$). During the first anodic scan, the release of Li^+ from $\text{Li}_x\text{C}/\text{Li}_x(\text{N-C})$ and the formation of Mo_xC mainly occur at $\approx 1.4 \text{ V}$. In the subsequent cycles, a pair of redox peaks centered at $\approx 1.4 \text{ V}$ (e.g., $\text{Mo}_x\text{C} \leftrightarrow \text{Li}_x\text{C} + \text{Mo}$) can be observed for all the $\text{Mo}_x\text{C@N-C-1.5}$ (Figure S5b, Supporting Information), $\text{Mo}_x\text{C@N-C-2.5}$ (Figure 4b) and $\text{Mo}_x\text{C@N-C-3.5}$ (Figure 4d). The highly overlapped CV curves for these $\text{Mo}_x\text{C@N-C}$ electrodes further indicate $\text{Mo}_x\text{C@N-C}$ with stable structures during the cycling.

Figure 4e presents the rate capability measurements of the electrodes at various current rates from 0.05 to 5 A g^{-1} between

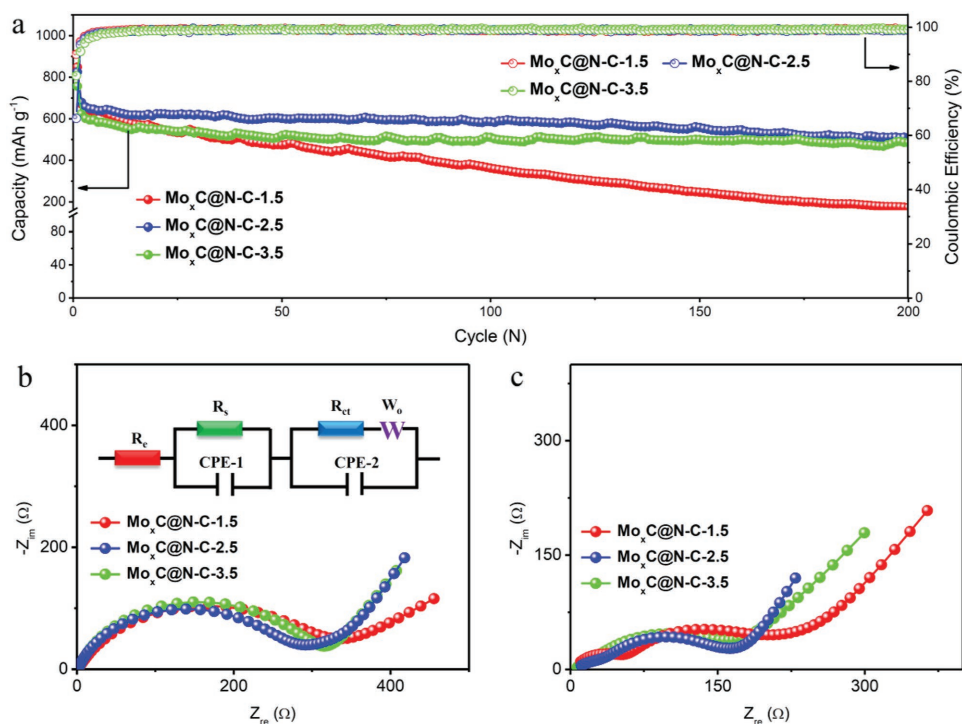


Figure 5. a) Cycling performance at 0.5 A g⁻¹ and electrochemical impedance spectra b) before cycling and c) after 200 cycles of Mo_xC@N-C-1.5, Mo_xC@N-C-2.5, and Mo_xC@N-C-3.5.

0.02 and 3 V. At 0.05 A g⁻¹, the Mo_xC@N-C-2.5 displays a much higher initial discharge capacity of 1254.4 mAh g⁻¹, followed by Mo_xC@N-C-3.5 (1002.6 mAh g⁻¹) and Mo_xC@N-C-1.5 (933.5 mAh g⁻¹), than Mo₂C (99.8 mAh g⁻¹). The higher capacities for Mo_xC@N-C than Mo₂C are mainly attributed to their rich active sites for Li⁺ storage. It should be noted that the initial Coulombic efficiencies of Mo_xC@N-C-2.5 (70.1%) and Mo₂C (69.3%) are lower than for Mo_xC@N-C-1.5 (95.3%) and Mo_xC@N-C-3.5 (86.9%), which is mainly due to the formation of different irreversible SEI layers. When the current density is progressively ramped from 0.05 to 5 A g⁻¹, the Mo_xC@N-C-2.5 exhibits the similar rate capability to Mo_xC@N-C-3.5 but higher than Mo_xC@N-C-1.5 (inset of Figure 4e). This is most likely due to the higher electronic conductivity of Mo_xC@N-C-2.5 and Mo_xC@N-C-3.5 with appropriate coating content and high crystallinity of N-C, compared to Mo_xC@N-C-1.5. As a result, the Mo_xC@N-C-2.5 delivers high average reversible capacity of 838.7, 728.0, 625.2, 535.7, 422.0, and 266.6 mAh g⁻¹ at 0.1, 0.25, 0.5, 1, 2.5, and 5 A g⁻¹, respectively. When the current density is back to 0.05 and 0.1 A g⁻¹, the reversible capacities of all the samples almost recover to their initial values, once again indicating their stable structures during the cycling.

To further evaluate long-term cycling stability of Mo₂C, Mo_xC@N-C-1.5, Mo_xC@N-C-2.5, and Mo_xC@N-C-3.5, the electrodes were measured at 0.5 A g⁻¹ for 200 cycles (Figure 5a). As can be seen, in the first cycle, the Mo_xC@N-C-1.5, Mo_xC@N-C-2.5, and Mo_xC@N-C-3.5 deliver initial discharge capacities of 763.2, 825.3, and 766.8 mAh g⁻¹. After 200 cycles, they maintain high discharge capacities of 172.9, 510.8, and 490.8 mAh g⁻¹ after 200 cycles with initial capacity retentions of 22.7%, 61.9%, and 64.0%, respectively, indicating more superiority of

Mo_xC@N-C-2.5 and Mo_xC@N-C-3.5 than Mo_xC@N-C-1.5. In order to further investigate their electrochemical kinetics, electrochemical impedance spectroscopy (EIS) of the Mo_xC@N-C cells measured at 0.5 A g⁻¹ before (Figure 5b) and after 200 cycles at fully charged state (Figure 5c) were compared. The equivalent circuit model is illustrated in inset of Figure 5b. The EIS spectra of the cycled electrode often include two semicircles at high-medium frequency, and a straight line at low frequency, corresponding to the SEI resistance (R_s) and charge transfer resistance (R_{ct}), and the Warburg (W_o) resistance, respectively.^[5,36] The value of R_{ct} (approximately equal to the numerical value of diameter of semicircle) is a key indicator of electrode kinetic. Before the cycling, all the Mo_xC@N-C electrodes without the formation of SEI layer show only a semicircle (R_{ct}) in the high-medium frequency region. After 200 cycles, all the Mo_xC@N-C electrodes present distinct double semicircles. Based on the fabricated equivalent model, the R_{ct} (second semicircle) of Mo_xC@N-C-1.5, Mo_xC@N-C-2.5, and Mo_xC@N-C-3.5 after 200 cycles are apparently decreased from 310.6, 256.7, and 288.5 Ω to 155.1, 98.2, and 109.6 Ω, respectively. The decreased R_{ct} is mainly due to electrode–electrolyte activation after discharge/charge cycling. Overall, the Mo_xC@N-C-2.5 shows the lowest R_{ct} among the Mo_xC@N-C series, indicating its strong electrochemical kinetic. These results are consistent with their corresponding electrochemical performance.

In summary, we have designed and synthesized a series of cross-linked macroporous Mo_xC@N-C nanocrystals through a simple method. The Mo_xC@N-C nanocrystals exhibit remarkable lithium storage properties, which can be mainly attributed to the presence of numerous active sites and unique 3D nanostructures. A large number of active sites with the enhanced

specific activity for Li⁺ storage are induced by the introduction of Mo vacancies to molybdenum carbides and nitrogen doping in carbon (N-C). The unique 3D nanostructures with large accessible surface area, cross-linked frameworks, and porous structures are beneficial for the quick penetration of the electrolyte, rapid diffusion of ions, and prevention of the electrode aggregation during the cycles. In addition, the N-C coating on the surfaces of Mo_xC@N-C structures not only significantly enhance the conductivity but also effectively alleviate the destruction of SEI film and agglomeration of the electrode. As a result, the Mo_xC@N-C-2.5 displays an initial reversible capacity of 879.3 mAh g⁻¹ at 0.05 A g⁻¹. At 0.5 A g⁻¹, the Mo_xC@N-C-2.5 shows a high discharge capacity of 825.3 mAh g⁻¹ with an initial capacity retention of 61.9% after 200 cycles. As expected, the approach to fabricate Mo_xC@N-C nanocrystal with rich defects, numerous cross-linked macroporous structures, and efficient N-C coating may be a valuable way to the development of other anodes toward high-performance LIBs in future.

Supporting Information

Supporting Information is available from the Wiley Online Library or from the author.

Acknowledgements

S.L. and F.L. contributed equally to this work. The authors are grateful for financial support from the “Young Talent Fellowship” program through South China University of Technology, the NSFC Committee of China (Grant No. 51672086), the Science and Technology Bureau of Guangdong Government (Grant No. 2017B030308005), and the Creative Research Initiative (CRI, Grant No. 2014R1A3A2069102) Science Research Centre (SRC, Grant No. 2016R1A5A1009405) programs from the National Research Foundation (NRF) of Korea.

Conflict of Interest

The authors declare no conflict of interest.

Keywords

lithium-ion batteries, macroporous materials, Mo vacancies, molybdenum carbide, nitrogen doping

Received: February 13, 2018
Revised: March 7, 2018
Published online: April 26, 2018

- [1] J. B. Goodenough, K.-S. Park, *J. Am. Chem. Soc.* **2013**, *135*, 1167.
[2] N. Nitta, F. Wu, J. T. Lee, G. Yushin, *Mater. Today* **2015**, *18*, 252.
[3] L. Croguennec, M. R. Palacin, *J. Am. Chem. Soc.* **2015**, *137*, 3140.
[4] a) R. Raccichini, A. Varzi, S. Passerini, B. Scrosati, *Nat. Mater.* **2014**, *14*, 271; b) J. T. Xu, I. Y. Jeon, J. M. Seo, S. X. Dou, L. M. Dai, J. B. Baek, *Adv. Mater.* **2014**, *26*, 7317; c) S. Wu, R. Xu, M. Lu, R. Ge, J. Iocozzia, C. Han, B. Jiang, Z. Lin, *Adv. Energy Mater.* **2015**, *5*, 1500400.
[5] J. T. Xu, Y. Lin, J. W. Connell, L. M. Dai, *Small* **2015**, *11*, 6179.
[6] a) X. Zhou, Y.-X. Yin, L.-J. Wan, Y.-G. Guo, *Adv. Energy Mater.* **2012**, *2*, 1086; b) J. Song, M. Zhou, R. Yi, T. Xu, M. L. Gordin, D. Tang, Z. Yu, M. Regula, D. Wang, *Adv. Funct. Mater.* **2014**, *24*, 5904;
c) N. Liu, Z. Lu, J. Zhao, M. T. McDowell, H.-W. Lee, W. Zhao, Y. Cui, *Nat. Nanotechnol.* **2014**, *9*, 187.
[7] K. H. Seng, M.-H. Park, Z. P. Guo, H. K. Liu, J. Cho, *Angew. Chem., Int. Ed.* **2012**, *124*, 5755.
[8] W. Li, X. Sun, Y. Yu, *Small Methods* **2017**, *1*, 1600037.
[9] a) J. Sun, G. Zheng, H.-W. Lee, N. Liu, H. Wang, H. Yao, W. Yang, Y. Cui, *Nano Lett.* **2014**, *14*, 4573; b) Z. Yu, J. Song, M. L. Gordin, R. Yi, D. Tang, D. Wang, *Adv. Sci.* **2015**, *2*, 1400020.
[10] N. Wang, Z. Bai, Y. Qian, J. Yang, *Adv. Mater.* **2016**, *28*, 4126.
[11] A. Finke, P. Poizot, C. Guéry, L. Dupont, P.-L. Taberna, P. Simon, J.-M. Tarascon, *Electrochem. Solid-State Lett.* **2008**, *11*, E5.
[12] a) M. V. Reddy, G. V. Subba Rao, B. V. R. Chowdari, *Chem. Rev.* **2013**, *113*, 5364; b) Y. Zhao, X. Li, B. Yan, D. Xiong, D. Li, S. Lawes, X. Sun, *Adv. Energy Mater.* **2016**, *6*, 1502175.
[13] X. Xu, W. Liu, Y. Kim, J. Cho, *Nano Today* **2014**, *9*, 604.
[14] a) B. Zhao, R. Ran, M. Liu, Z. Shao, *Mater. Sci. Eng., R* **2015**, *98*, 1; b) T. Yuan, Z. Tan, C. Ma, J. Yang, Z.-F. Ma, S. Zheng, *Adv. Energy Mater.* **2017**, *7*, 1601625.
[15] B. Anasori, M. R. Lukatskaya, Y. Gogotsi, *Nat. Rev. Mater.* **2017**, *2*, 16098.
[16] Y. Jiao, Y. Zheng, M. Jaroniec, S. Z. Qiao, *Chem. Soc. Rev.* **2015**, *44*, 2060.
[17] M. Chen, J. Liu, W. Zhou, J. Lin, Z. Shen, *Sci. Rep.* **2015**, *5*, 10389.
[18] H. Fan, H. Yu, Y. Zhang, Y. Zheng, Y. Luo, Z. Dai, B. Li, Y. Zong, Q. Yan, *Angew. Chem., Int. Ed.* **2017**, *129*, 12740.
[19] F. Li, X. Zhao, J. Mahmood, M. S. Okyay, S.-M. Jung, I. Ahmad, S.-J. Kim, G.-F. Han, N. Park, J.-B. Baek, *ACS Nano* **2017**, *11*, 7527.
[20] M. Naguib, J. Come, B. Dyatkin, V. Presser, P.-L. Taberna, P. Simon, M. W. Barsoum, Y. Gogotsi, *Electrochem. Commun.* **2012**, *16*, 61.
[21] Q. Tang, Z. Zhou, P. Shen, *J. Am. Chem. Soc.* **2012**, *134*, 16909.
[22] M. Naguib, J. Halim, J. Lu, K. M. Cook, L. Hultman, Y. Gogotsi, M. W. Barsoum, *J. Am. Chem. Soc.* **2013**, *135*, 15966.
[23] O. Mashtalir, M. R. Lukatskaya, M.-Q. Zhao, M. W. Barsoum, Y. Gogotsi, *Adv. Mater.* **2015**, *27*, 3501.
[24] Z. Xu, X. Lv, J. Chen, L. Jiang, Y. Lai, J. Li, *Phys. Chem. Chem. Phys.* **2017**, *19*, 7807.
[25] J. Zhu, K. Sakaushi, G. Clavel, M. Shalom, M. Antonietti, T.-P. Fellingner, *J. Am. Chem. Soc.* **2015**, *137*, 5480.
[26] Q. Gao, X. Zhao, Y. Xiao, D. Zhao, M. Cao, *Nanoscale* **2014**, *6*, 6151.
[27] Y. Yang, X. Fan, G. Casillas, Z. Peng, G. Ruan, G. Wang, M. J. Yacaman, J. M. Tour, *ACS Nano* **2014**, *8*, 3939.
[28] H.-J. Zhang, K.-X. Wang, X.-Y. Wu, Y.-M. Jiang, Y.-B. Zhai, C. Wang, X. Wei, J.-S. Chen, *Adv. Funct. Mater.* **2014**, *24*, 3399.
[29] Q. Sun, Y. Dai, Y. Ma, T. Jing, W. Wei, B. Huang, *J. Phys. Chem. Lett.* **2016**, *7*, 937.
[30] a) Y. Xiao, L. Zheng, M. Cao, *Nano Energy* **2015**, *12*, 152; b) T. Meng, L. Zheng, J. Qin, D. Zhao, M. Cao, *J. Mater. Chem. A* **2017**, *5*, 20228; c) H. Yu, H. Fan, J. Wang, Y. Zheng, Z. Dai, Y. Lu, J. Kong, X. Wang, Y. J. Kim, Q. Yan, J.-M. Lee, *Nanoscale* **2017**, *9*, 7260.
[31] a) M. Ihsan, H. Wang, S. R. Majid, J. Yang, S. J. Kennedy, Z. Guo, H. K. Liu, *Carbon* **2016**, *96*, 1200; b) L. Yang, X. Li, Y. Ouyang, Q. Gao, L. Ouyang, R. Hu, J. Liu, M. Zhu, *ACS Appl. Mater. Interfaces* **2016**, *8*, 19987; c) C. Wang, L. Sun, F. Zhang, X. Wang, Q. Sun, Y. Cheng, L. Wang, *Small* **2017**, *13*, 1701246; d) H. Liao, H. Hou, Y. Zhang, X. Qiu, X. Ji, *ChemElectroChem* **2017**, *4*, 2669.
[32] J. Chen, Y. Huang, F. Zhao, H. Ye, Y. Wang, J. Zhou, Y. Liu, Y. Li, *J. Mater. Chem. A* **2017**, *5*, 8125.
[33] B. Wang, G. Wang, H. Wang, *J. Mater. Chem. A* **2015**, *3*, 17403.
[34] L. Yang, X. Li, S. He, G. Du, X. Yu, J. Liu, Q. Gao, R. Hu, M. Zhu, *J. Mater. Chem. A* **2016**, *4*, 10842.
[35] a) F. Zheng, Y. Yang, Q. Chen, *Nat. Commun.* **2014**, *5*, 5261; b) R. Mukherjee, A. V. Thomas, D. Datta, E. Singh, J. Li, O. Eksik, V. B. Shenoy, N. Koratkar, *Nat. Commun.* **2014**, *5*, 3710.
[36] J. T. Xu, J. Mahmood, Y. H. Dou, S. X. Dou, F. Li, L. M. Dai, J. B. Baek, *Adv. Mater.* **2017**, *29*, 201702007.
[37] X. Li, J. Zhang, R. Wang, H. Huang, C. Xie, Z. Li, J. Li, C. Niu, *Nano Lett.* **2015**, *15*, 5268.